King Saud University

Arabian Journal of Chemistry

www.ksu.edu.sa
www.sciencedirect.com

ORIGINAL ARTICLE

Precise regulation of Ultra-thin platinum decorated Gold/Graphite carbon nitride photocatalysts by atomic layer deposition for efficient degradation of Rhodamine B under simulated sunlight

Hongfen Zhang [1],[*], Baiyan Zhang [1], Fangmiao Liang, Yang Fang, Hong Wang, Anjia Chen

School of Pharmacy, Shanxi Medical University, Jinzhong 030619, Shanxi, China

Abstract Atomic Layer Deposition (ALD) precise controlling ultra-thin platinum (Pt) modified Graphite carbon nitride (g-C_3N_4) photocatalysts, which had been doped with gold nanoparticles (Au NPs) by photodeposition, were successfully synthesized. The experimental results showed that precise regulation of platinum decorated C_3N_4-Au(C_3N_4-Au/nPt (n is the number of Pt ALD cycles, 1 Å per cycle)) exhibited excellent photocatalytic degradation ability for Rhodamine B (RhB). Under simulated sunlight irradiation, the degradation rate of 10 mg/L RhB(100 mL) by 1.5 mg C_3N_4-Au/10Pt catalysts was 95.8% within 60 min that is much better than other photocatalysts for the degradation of RhB. The efficient degradation mechanism of RhB by C_3N_4-Au/10Pt photocatalysts was studied and the experiments demonstrated the $\cdot O_2^-$ as main active species played an important role in the photocatalytic process. Local surface plasmon resonance (LSPR) of Au NPs and Schottky barrier between Pt clusters and g-C_3N_4 may be the reasons for enhanced C_3N_4-Au/10Pt photocatalytic performances. Furthermore, the successive catalytic cycles revealed the excellent stability of C_3N_4-Au/10Pt photocatalyst.

© 2022 The Author(s). Published by Elsevier B.V. on behalf of King Saud University. This is an open access article under the CC BY-NC-ND license (http://creativecommons.org/licenses/by-nc-nd/4.0/).

1. Introduction

The global energy crisis and environmental issues have spurred the search for clean and renewable energy source to replace conventional coal, oil and gas. Photocatalysis, using inexhaustible solar energy, is a powerful tool to solve the worldwide energy shortage, environmental contamination and the greenhouse effect (Meng et al., 2016, Jinlong et al., 2019, Eshwar et al., 2020). Among many photocatalysts that have

* Corresponding author.
  E-mail address: zhanghf_2007@126.com (H. Zhang).
[1] These authors contributed equally to this work.
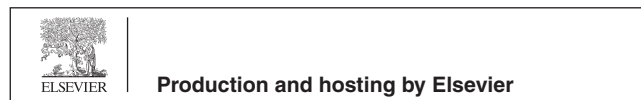
been developed, graphitic carbon nitride (g-C$_3$N$_4$) has become an attractive visible-light catalyst owing to its numerous qualities such as simple preparation, electrochemical properties, abundance, nontoxicity and chemical tenability (Ya-Nan et al., 2017, Taehwan et al., 2019, Mohammed et al., 2020). For example, g-C$_3$N$_4$ has a bandgap of 2.7 eV which can lead itself to be an excellent visible light responsive photocatalyst (Mamba and Mishra 2016, Li et al., 2021, Wenjun et al., 2021). The g-C$_3$N$_4$ materials lead to multiple excitation after single-photon absorption, producing a large number of active substances (such as ·O$_2^-$, ·OH, etc.), degrading organic pollutants, killing bacteria and reducing carbon dioxide (Amene et al., 2017, Dilshad et al., 2017, Guohui et al., 2017, Jingrun et al., 2018).

However, the photocatalytic efficiency of g-C$_3$N$_4$ is still not ideal due to its limited visible-light capture ability (about 460 nm with absorption edge), high charge carrier recombination rate and low surface area (Yanchun et al., 2020). Thus, various modification methods were used to improve photocatalytic performance of g-C$_3$N$_4$-based materials, such as elemental and molecular doping to narrow the bandgap for enhancing the absorption of visible light (Wee-Jun et al., 2016, Yanchun et al., 2020), structuring composite with cocatalysts to improve the catalytic kinetics (Juan et al., 2015, Sibo et al., 2019), the formation of heterojunction with other semiconductors to improve light response (Noor Izzati Md et al., 2021, Xu et al., 2021, Yan et al., 2021) and the introduction of substrates with excellent carrier mobility to make better charge extraction efficiency (Min-Ying et al., 2012, Wee-Jun et al., 2015).

Designing the electronic structure of g-C$_3$N$_4$ by doping, loading and hybridizing with metal atoms (e.g., Au, Ag, Zn, Pt and Cu) is an important strategy to improve the performance of g-C$_3$N$_4$ (Xinchen et al., 2009, Zhengxin et al., 2010, Jingqi et al., 2013, Surendar et al., 2014, Trishamoni et al., 2021, Noor Izzati Md et al., 2022). For instance, Sun et al. (Ningyan et al., 2013) reported that the nanohybrids of Au-loaded g-C$_3$N$_4$ nanosheets showed superior photocatalytic activities for the decomposition of methyl orange (MO) under visible-light irradiation to bulk g-C$_3$N$_4$ and g-C$_3$N$_4$ nanosheets. Very recently, novel ZnO/Au/g-C$_3$N$_4$ nanocomposites were prepared by a liquid-phase pulsed laser method followed by calcination (Seung Jun et al., 2020). The ZnO/Au/g-C$_3$N$_4$ nanocomposites showed enhanced catalytic activity for the degradation of methylene blue (MB) under simulated sunlight. A novel plasmonic photocatalyst, Au/Pt/g-C$_3$N$_4$, was prepared by a facile calcination-photodeposition technique. The Au/Pt decorated g-C$_3$N$_4$ heterostructure displayed enhanced photocatalytic activity for antibiotic tetracycline hydrochloride (TC-HCl) degradation. The degradation rate was 3.4 times higher than that of pure g-C$_3$N$_4$ under visible light irradiation (Jinjuan et al., 2015). However, the above methods in the synthetic process of g-C$_3$N$_4$-based nanocomposites are difficult to accurately control the size, distribution and loading capacity of metal atoms. Therefore, it is essential to develop new strategies to accurately design nano-photocatalysts from a single atom to clusters with specific atomic numbers and unique complex structures, in order to improve photocatalytic activity under sunlight.

Atomic layer deposition (ALD) is a thin film preparation technology that originated in Finland in the 1970 s. ALD has the advantages of self-limiting, atom-by-atom growth and a variety of materials that can be deposited. It is an ideal method for the precise design of metal nano-photocatalysts with adjustable atomic numbers (Jie et al., 2021). ALD technology also can control the thickness of monolayer, submonolayer and angstrom level to engineer the formation and growth of surface layer sediments at the atomic level (Zhe and Yong 2017, Jiankang et al., 2019, Ji-Xiao et al., 2020, Jie et al., 2021).

Here, we developed a new strategy to modulate Pt nucleation and growth by ALD to precisely tailor g-C$_3$N$_4$-based nano-photocatalysts (see Schematic diagram 1) for achieving superior photocatalytic performance by downsizing Pt nanocatalysts at the sub-nanometric size (cluster and a single atom). The precise controlling g-C$_3$N$_4$-based nano-photocatalysts as-obtained (expressed as C$_3$N$_4$-Au/nPt, n for the number of Pt ALD cycles) were characterized by transmission electron microscopy (TEM), X-ray photoelectron spectroscopy (XPS), Fourier-transform infrared spectroscopy (FTIR), UV–vis diffuse reflectance spectra (UV–vis DRS) and electrochemical methods. All the experimental results confirmed that platinum was precisely designed on the surface of Au/C$_3$N$_4$, where g-C$_3$N$_4$ had been doped with Au by photodeposition. The C$_3$N$_4$-Au/10Pt nano-photocatalysts exhibited an outstanding efficient degradation of Rhodamine B (RhB) under simulated sunlight. Theoretical and experimental studies were carried out to investigate the origin of this highly efficient photocatalytic performance. The precisely regulated C$_3$N$_4$-Au/nPt photocatalysts were first synthesized by ALD and successfully applied in the efficient degradation of RhB. The results of this paper provide a hopeful prospect for the application of precisely controlled g-C$_3$N$_4$-based nanomaterials with metal atoms in the degradation of organic pollutants under sunlight.

2. Experimental details

2.1. Materials

All reagents were analytically pure and can be used without further purification. Deionized water was used in all experiments. Chloroauric acid and Trimethyl (methylcyclopentadienyl) platinum (MeCpPtMe$_3$, 99%) were purchased from Alfa Aesar, USA. Urea was obtained from Sinopharm Chemical Reagent Co., Ltd. Disodium ethylenediaminetetraacetic acid (EDTA-2Na) was purchased from Beijing Suolaibao Technology Co., Ltd. NaOH, NaH$_2$PO$_4$, concentrated sulfuric acid, isopropanol (IPA) and ascorbic acid (AA) were obtained from Tianjin Damao Chemical Reagent Co., Ltd.

2.2. Synthesis of g-C$_3$N$_4$

40 g urea powder was put into a porcelain crucible with a lid and heated from room temperature to 500 °C at a rate of 10 °C min^{-1} in a Ksl-1100x muffle furnace (Hefei keying Material Technology Co., Ltd), and kept for 4 h, then cooled naturally to room temperature. The bulk g-C$_3$N$_4$ was obtained and ground for 3 min to obtain a fine powder. The g-C$_3$N$_4$ (C$_3$N$_4$ for short) prepared at 600℃ and 700℃ were prepared by the same way. The C$_3$N$_4$ synthesized at 800℃ was stored for 10 min in a muffle furnace, then cooled naturally to room temperature.
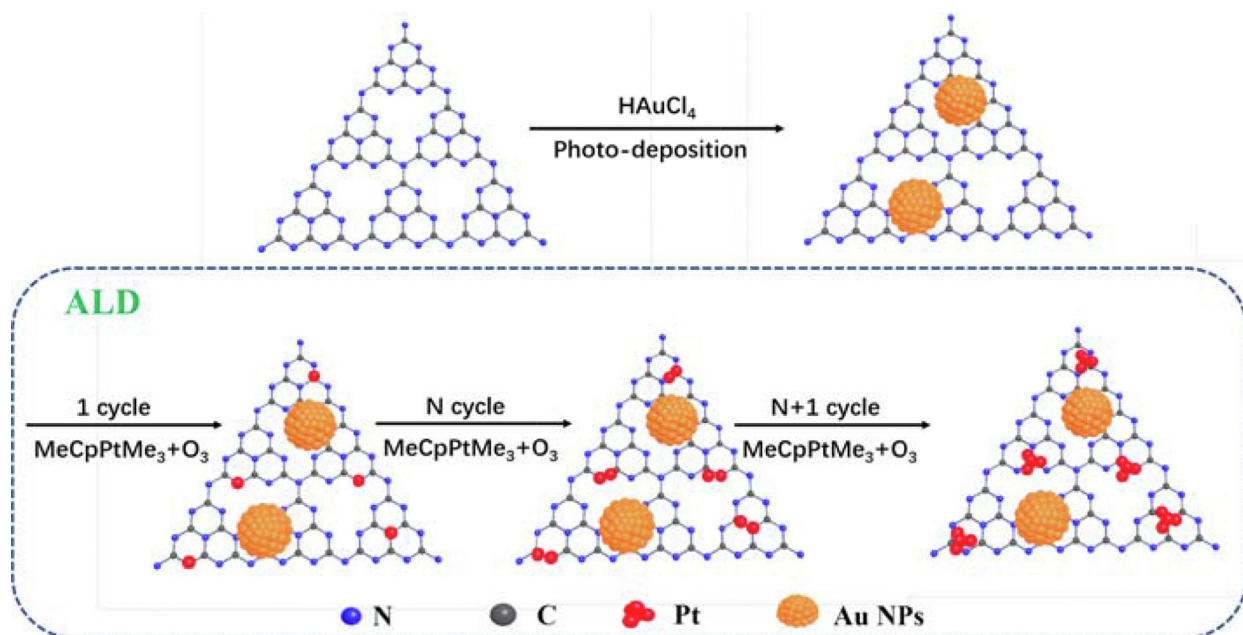
Scheme 1 Schematic illustration of synthetic processes for precisely controlled C_3N_4-Au/nPt nano-photocatalysts by ALD.

2.3. Fabrication of C_3N_4-Au by photodeposition method

Firstly, 165 μL of chloroauric acid (0.1 g·mL^{-1}), 150 mg of carbon nitride and 15 mL of methanol were added into a photoreactor containing 60 mL of deionized water, respectively. Then, the above-mentioned mixed solution was stirred for 3 h under a CEL-HXF300-T3 xenon lamp (Beijing Zhongjiao Jinyuan Technology Co., Ltd). Lastly, C_3N_4-Au was prepared after being filtered by suction filtration (Millipore Filter Membrane, Water-system, 0.45 μm, Shanxi mini bio NG-1345 W) and dried at 60℃ for 6 h under the condition of vacuum.

2.4. Fabrication of sub-nanometric photocatalyst (C_3N_4-Au/ nPt) by ALD

Pt was precisely engineered on the as-prepared C_3N_4-Au, which was dispersed on a quartz surface of $8.0 \times 8.0 \times 0.2$ cm^3, using MeCpPtMe$_3$ and O$_3$ generated from a CF-G-3–5 g ozone generator (Qingdao Garden Environmental Protection Technology Co., Ltd) as precursors at 280 °C in the same self-developed atomic layer deposition system (Self-developed by Institute of Shanxi Coal Chemistry, Chinese Academy of Sciences). MeCpPtMe$_3$ was maintained at 68℃ to provide adequate steam pressure. For each ALD cycle, the pulse, exposure, and purge times for MeCpPtMe$_3$ were 1, 15 and 25 s, respectively, and those of O$_3$ were 1, 12 and 20 s, respectively. Nitrogen (99.999%) was used as the carrier and purge gas. Different Pt ALD cycles were performed to obtain a series of catalysts with precisely controlled Pt sizes and loads (expressed as C_3N_4-Au/nPt, n for the number of Pt ALD cycles). Under the same ALD conditions, different cycles of Pt ALD were carried out on the g-C_3N_4 substrate (expressed as C_3N_4/xPt, x is the number of Pt ALD cycles) as the control experiments.

2.5. Characterizations of catalysts

The morphology and crystalline structure of the samples were determined by TEM, high resolution TEM (HRTEM) and EDS profiles on a JEOL-2100F microscope operated at 200 kV. The crystal structure of the samples were confirmed by X-ray diffraction (XRD) with Cu Kα radiation (λ = 1.540 Å, Bruker D8 Advance X-ray diffractometer). The XPS of the samples were measured by ESCALAB250Xi photoelectron spectrometer equipped with Al Kα source (hν = 1486.6 eV). The binding energy is calibrated at 248.8 eV. The functional groups on the surface of the materials were scanned at $400 \sim 4000$ cm^{-1} by Fourier Transform infrared spectrometer (Nicolet iS5). A Thermo Scientific Evolution 220 spectrophotometer was used to record the diffuse reflection ultraviolet–visible spectra (UV–vis DRS) in the range of 200–800 nm with BaSO$_4$ as the background to characterize the light absorption performance of the samples.

2.6. Photocatalytic experiments

The photocatalytic performances of the as-prepared photocatalysts were evaluated by RhB degradation under simulated sunlight irradiation. Photocatalysts (1.5 mg) were introduced into 100 mL RhB solution (10 mg·L^{-1}) and dispersed under ultrasonic dispersion for 30 min. Then, the systems were magnetically stirred in the dark for 20 min to reach the adsorption–desorption equilibrium prior to light irradiation. A 300 W xenon lamp with the current intensity of 14 A was used as the light source. The sampling frequency by a syringe was 5 min and all the samples were filtrated through a 0.45 μm cellulose acetate membrane to remove the catalysts particles. The simulated sunlight irradiation time was 30 min. 2 mL of the clarified solution was analyzed using a U-3900 UV–vis spec-

trophotometer (Hitachi, Japan) and the maximum absorbance wavelength of RhB was 550 nm. Degradation efficiency and photocatalytic rate kinetics were determined by the following equations (1) and (2), which are:

$$Degradation\ efficiency\ (DE\ \%) = \frac{C_0 - C_t}{C_0} \times 100$$

$$= \frac{A_0 - A_t}{A_0} \times 100 \qquad (1)$$

$$Ln\left(\frac{C_0}{C_t} = \frac{A_0}{A_t}\right) = Kt \qquad (2)$$

where C_0 and A_0 are the initial concentration and absorbance of RhB, while C_t and A_t are the concentration and absorbance of RhB at the reaction time t (min), respectively. k (min^{-1}) is the rate constant, and t (min) is the time of photocatalytic degradation.

2.7. Photoelectrochemical measurement

Electrochemical measurements were performed by using the CHI660E electrochemical workstation (Shanghai ChenHua Instrument Co., Ltd.). The electrochemical analyzer has a standard three-electrode system, in which the synthesized samples coated on F-doped SnO$_2$-coated glass (FTO glass) as the working electrodes, a Pt wire was used as the counter electrode and saturated calomel electrode (SCE) used as a reference electrode. The Electrochemical impedance spectroscopy (EIS) frequency range was from 0.005 to 10^6 Hz with amplitude of 10 mV. Transient photocurrents (TPC) were performed in the same three-electrode system. The preparation of working electrodes was as follows: 0.1 g of the photocatalysts was mixed with 5 mL of ethanol and ultrasonically dispersed for 30 min to form a uniformly dispersed liquid. The 10 μL of the above-mentioned dispersion liquid was coated onto a 2.0 × 2.0 cm^2 FTO glass electrode directly. The obtained electrodes were dried in an oven and heated in a nitrogen stream at 300 °C for half an hour. The film diameter of all electrodes used was approximately 6 mm.

3. Results and discussion

3.1. Characterization of synthesized photocatalysts

To confirm the successful loading Au NPs and Pt clusters on the surface of C$_3$N$_4$ via photodeposition and ALD methods, the morphology, composition and chemical states of C$_3$N$_4$-Au/10Pt were investigated. The TEM images of C$_3$N$_4$-Au/10Pt are shown in Fig. 1. The well dispersed Au NPs are closely combined with C$_3$N$_4$ in Fig. 1a, which is beneficial for transferring of photo-induced electrons in Au NPs to C$_3$N$_4$ by Localized Surface Plasmon Resonance (LSPR) (Chuang et al., 2017). In Fig. 1b, the fringe with the interplanar spacing of 0.235 and 0.205 nm is assigned to the (1 1 1) and (1 0 0) crystal plane of Au NPs, respectively (Ji-Xiao et al., 2020). However, Pt clusters could not be observed neither in TEM nor in HRTEM after being decorated on C$_3$N$_4$-Au by ALD, which is due to the high dispersion of ALD method (Zhe and Yong 2017) and low platinum loading (0.26 at.% in Fig. 1c and Table 1). Elemental composition of C$_3$N$_4$-Au/10Pt in Fig. 1c revealed that as-synthesized catalyst

was composed of C, N, Au, and Pt elements, providing evidence for the successful formation of C$_3$N$_4$-Au/10Pt photocatalysts.

The chemical composition and crystal structure of C$_3$N$_4$-Au/10Pt were studied by XRD patterns. In Fig. 1d, two representative diffraction peaks located at 13.7° and 27.8°, which can be indexed as the in-plane periodic repeat structural and conjugated aromatic systems in (1 0 0) and (0 0 2) graphitic plane of carbon nitride, respectively (Ning et al., 2017, Yanchun et al., 2020, Yiping et al., 2020). The diffraction peaks at 38.4°, 44.7°, 64.9°, 77.8° and 81.3° were attributed to the (1 1 1), (2 0 0), (2 2 0), (3 1 1) and (2 2 2) diffraction faces of the Au species, respectively (Xin et al., 2019). However, no peak belonged to Pt, indicating Pt species was too small and highly dispersed. The result was consistent with the TEM results.

The XPS spectra were applied to elucidate the chemical states and the interactions between components in bare C$_3$N$_4$ and C$_3$N$_4$-Au/10Pt. Table 1 and Fig. 2a exhibit that there are C1s, N1s, O1s, Au 4f and Pt 4f in C$_3$N$_4$-Au/10Pt, which are consistent with EDS results. During the deposition of platinum clusters by ALD, these increased oxygen species that oxidized by O$_3$ pulse, namely O-H, C-O, C = O and O-C = O, which further induced the nucleation of Pt on C$_3$N$_4$-Au (Fig. 2b) (Jie et al., 2021). The C1s spectra in Fig. 2c are divided into two peaks located on 284.8 eV and 288.3 eV, which are ascribed to the graphitic carbon and N = C-N bounding in the triazine framework, respectively (Kwun-Han et al., 2017, Yanchun et al., 2020). Moreover, the N1s spectra (Fig. 2d) show three peaks at 398.7, 399.6 and 400.6 eV for C$_3$N$_4$, which are ascribed to the C-N = C, N(C)$_3$ and NH$_X$ in the triazine framework, respectively. The C1s and N1s spectra indicate C$_3$N$_4$ is a triazine framework. Compared with C$_3$N$_4$, C$_3$N$_4$-Au/10Pt exhibited new functional groups of N-C = O, indicating that a part of N is replaced by O in C$_3$N$_4$-Au/10Pt, which is consistent with the increase of O contents shown in Fig. 2b and Table 1. Moreover, the peaks for C-N = C, N(C)$_3$ and NH$_x$ shift to higher binding energy at 398.8, 400.2 and 401.2 eV after Au NPs and Pt clusters decoration, respectively. This is because the nitrogen groups with high local electron density in C$_3$N$_4$ can provide lone pair electrons to the empty d orbitals of the Pt atoms, thus stabilizing Pt through strong metal-carrier interaction and leading to its high distribution (Shaowen et al., 2016). Meanwhile, two characteristic peaks at 83.3 and 87.5 eV were observed in Fig. 2e, originating from metallic Au 4 f5/2 and Au 4f7/2, respectively (Xin et al., 2019). In Pt 4f spectra of C$_3$N$_4$-Au/10Pt (Fig. 2f), a tremendous amount of Pt exists in the form of high valence state, which indicates a large number of Pt atoms binding with N atoms in C$_3$N$_4$ (Xiaogang et al., 2016).

FTIR was used to analyze the chemical bonds in the samples. In Fig. 3a, the FTIR spectra of all these samples have similar chemical bond at 811 cm^{-1} (the breathing smode of the tris-triazine system) and 890 cm^{-1} (the deformation mode of N-H), 1200–1700 cm^{-1} (C-N and C = N stretching vibration modes) and 3000–3500 cm^{-1} (O-H and N-H stretching vibration modes) (Kwun-Han et al., 2017, Yanchun et al., 2020). These results indicate that triazine framework structure remained mostly unchanged after the modification of Au NPs and Pt clusters. Fig. 3b illustrates the UV–vis DRS of the samples. The absorption edges of C$_3$N$_4$, C$_3$N$_4$-Au and C$_3$N$_4$-Au/10Pt have a little difference, suggesting that the decoration
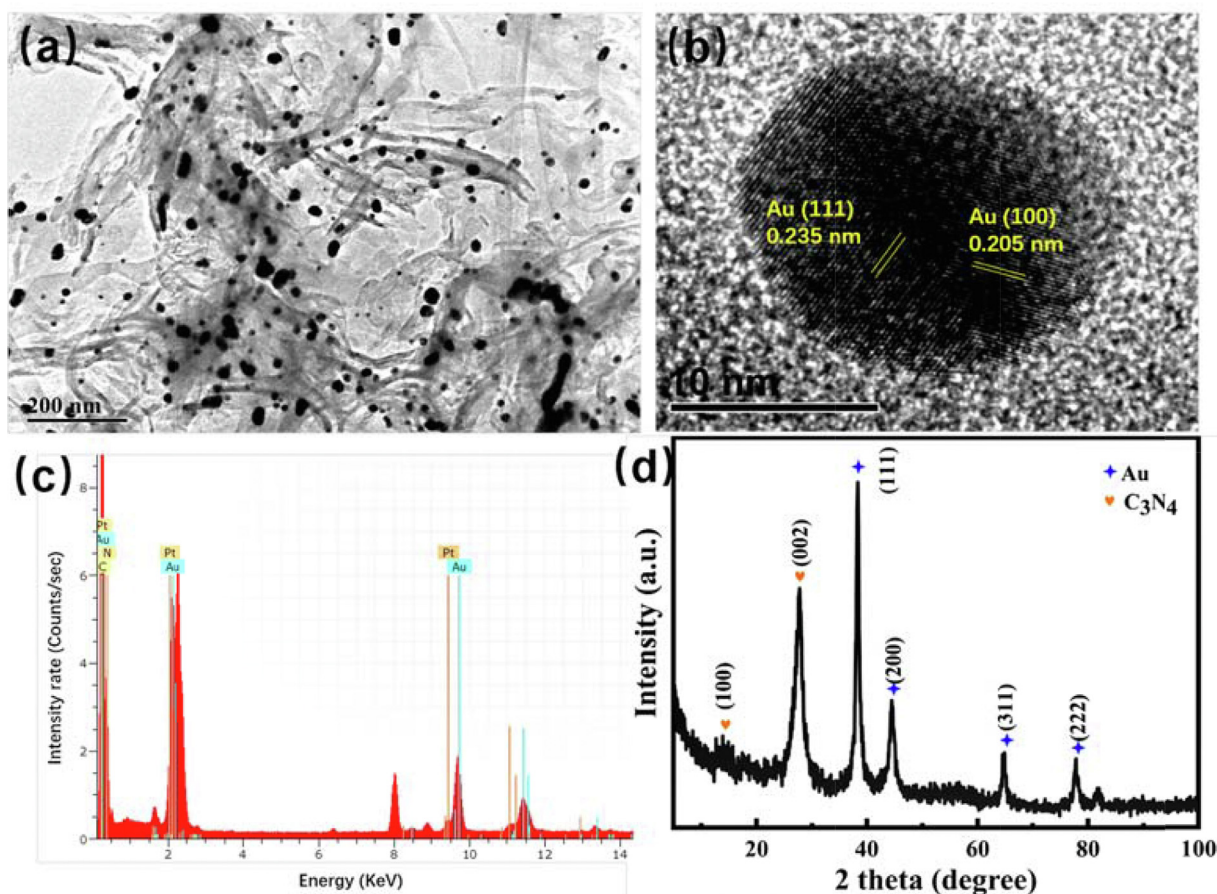
Fig. 1 TEM images of C_3N_4-Au/10Pt (a), HRTEM of Au NPs (b), EDS (c) and XRD pattern of C_3N_4-Au/10Pt(d).

Table 1 Each element content in C_3N_4 and C_3N_4-Au/10Pt based on XPS results.

Photocatalyst	C 1 s	N 1 s	O 1 s	Au 4f	Pt 4f
C_3N_4	44.47%	55.22%	2.31%		
C_3N_4-Au/10Pt	40.92%	54.31%	4.31%	0.21%	0.26%

of Au NPs and Pt clusters modified on C_3N_4, which are consistent with XPS, XRD and TEM results. Compared with C_3N_4, strong photo-absorption was observed at approximately 550 nm in C_3N_4-Au and C_3N_4-Au/10Pt, which was attributed to the LSPR effect of Au NPs on C_3N_4 (Zhi Wei et al., 2012, Xin et al., 2019). In addition, the whole increase of light absorption intensity in the relatively wide range ($\lambda > 420$ nm) is caused by the scattering of Pt clusters on C_3N_4 (Shaowen et al., 2016). Moreover, the band gap values of the synthesized samples were calculated as 2.87 eV, 2.94 eV and 2.94 eV, respectively (Fig. 3c) by Kubelka-Munk formula (Yuyang et al., 2015, Yong et al., 2018, Yuan et al., 2020):

$$(\alpha h\nu)^2 = A(h\nu - E_g) \tag{3}$$

where α represents absorption coefficient, h is Planck constant, A is a constant, ν is the ratio of wavelength to speed of light (c), E_g represents band gap. As shown from Fig. 3c, the deco-

ration of Au NPs and Pt clusters can enhance visible light absorption.

The EIS spectra and photocurrent-time response were implemented to investigate the charge separation and transfer performance of C_3N_4-Au/10Pt. Fig. 4a showed that the arc radii of the samples increase in the order C_3N_4-Au/10Pt < C_3N_4-Au < C_3N_4, which indicated C_3N_4-Au/10Pt owns the smallest impedance in the photocatalytic process. Compared with C_3N_4 and C_3N_4-Au, C_3N_4-Au/10Pt showed a significantly enhanced photocurrent density, further verifying C_3N_4-Au/10Pt exhibited higher charge separation and transfer efficiency (see Fig. 4b). These results indicated that the Au NPs and Pt clusters could synergistically attribute the separation and transfer of carriers.

3.2. Photocatalytic activity and stability

The photocatalytic activities of the as-prepared samples were evaluated by degrading RhB dye in simulated sunlight. As
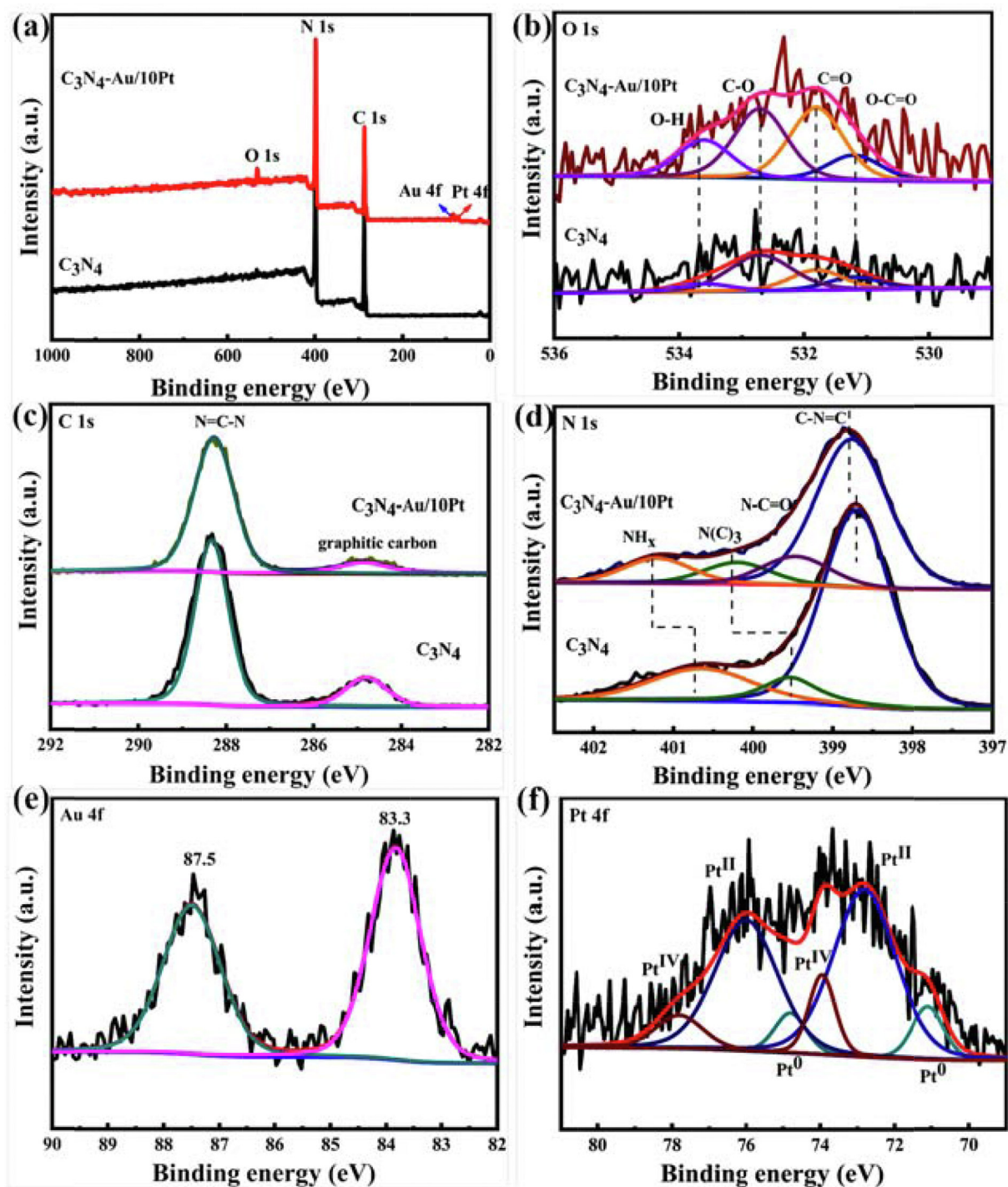
Fig. 2 XPS survey spectra (a) and high-resolution XPS spectra of O 1 s (b), C 1 s (c), N 1 s (d), Au 4f (e) and Pt 4f (f) for bare C_3N_4 and C_3N_4-Au/10Pt.

can be seen from Fig. 5a, the degradation rate of RhB dye without catalyst was almost unchanged after simulated sunlight irradiation for 30 min. However, when the synthesized C_3N_4 photocatalysts were added, the degradation efficiency of RhB was higher than that without photocatalysts (see Fig. 5), which demonstrated that the as-prepared C_3N_4 catalysts had good photocatalytic activities. In order to find out the optimal synthesis temperature of C_3N_4, the effects of dif-

ferent synthesis temperatures such as 500 ℃, 600 ℃, 700 ℃ and 800 ℃ on the degradation of RhB under simulated sunlight irradiation were studied. The experimental results showed that the activities of synthesized photocatalysts were all good apart from 800 ℃. It was reported that a large amount of ammonia was released during the pyrolysis of urea (Liu et al., 2011). The released ammonia gas filled and eroded the system of carbon nitride, forming a microporous structure
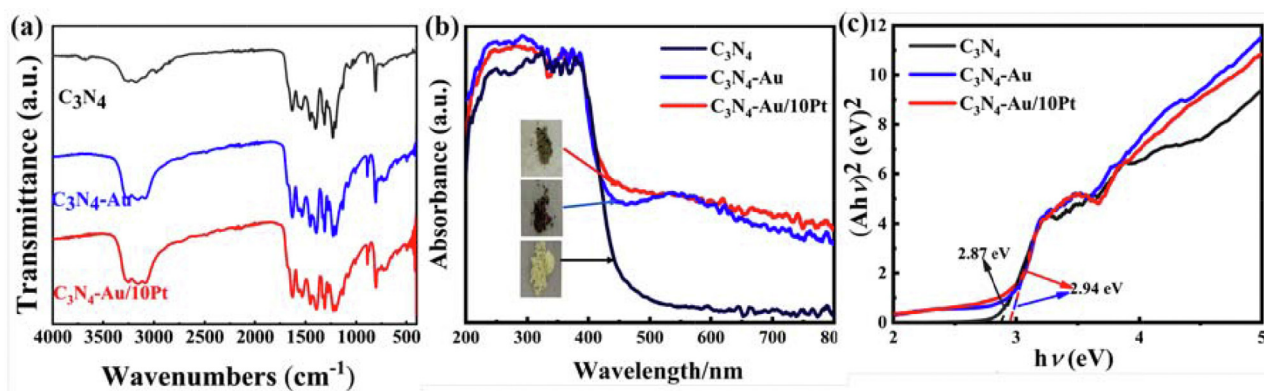
Fig. 3 FTIR absorption spectra (a), Diffuse reflectance spectra(b) Tauc plots (c)of C_3N_4, C_3N_4-Au and C_3N_4-Au/10Pt.
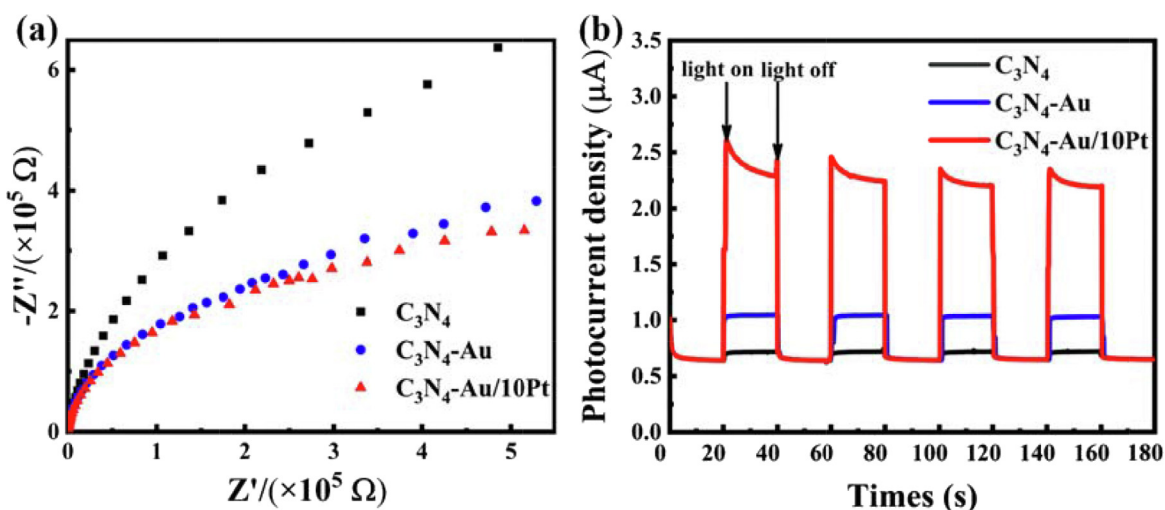

Fig. 4 EIS spectra (a) and photocurrent responses(b) of C_3N_4, C_3N_4-Au and C_3N_4-Au/10Pt.
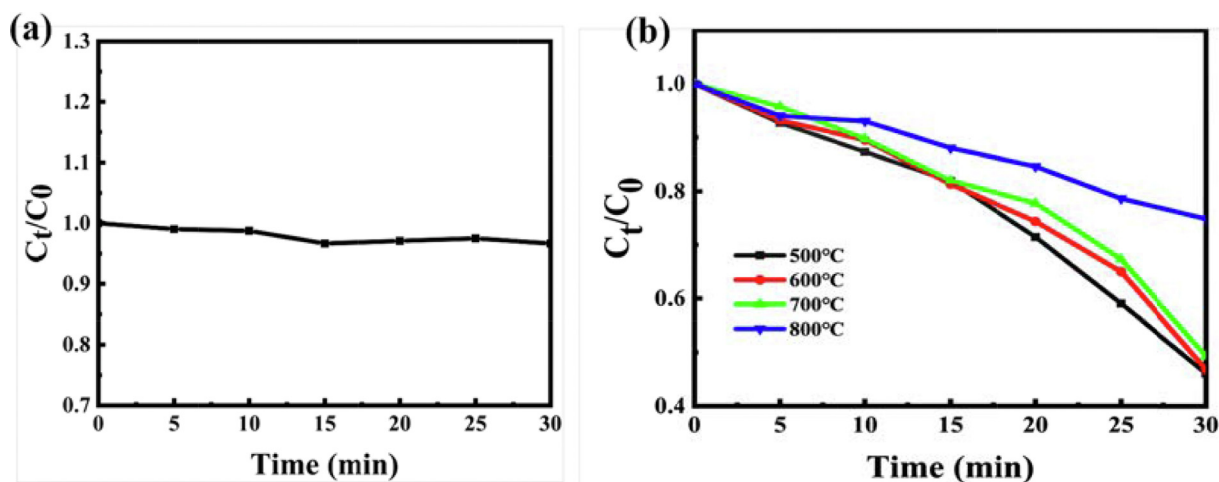

Fig. 5 Degradation efficiency of RhB without (a) and present (b) catalysts with different calcinated temperature under sunlight irradiation.

and increasing the specific surface area of the carbon nitride. The larger specific surface area and more mesoporous structure will be favorable for C_3N_4 to adsorb organic dyes and sunlight (Fan et al., 2013). However, 800℃ was maybe too high for urea to break down into ammonia and H_2O, which led to the poor photocatalytic activity of C_3N_4. And more

defeats in C_3N_4 under 800℃ calcination increase non-radiative recombination rates of the carriers (Po et al., 2014). According to the experimental results (see Fig. 5b), photocatalysts of C_3N_4 synthesized at 500℃ was finally used for the subsequent tests.

By controlling the number of Pt ALD cycles on the C_3N_4-Au, a series of precisely regulated Pt sub-nano catalysts were synthesized (see Schematic diagram 1). As a model reaction, the photocatalytic degradation of RhB aqueous solution by C_3N_4, C_3N_4-Au, xPt/C_3N_4 and C_3N_4-Au/nPt photocatalysts was further studied. As shown in Fig. 6a, during the 30-minute photoreaction process, different photocatalysts have different photocatalytic degradation rates for RhB. Among them, C_3N_4-Au/10Pt has the fastest degradation rate of RhB with a degradation rate of 86.3%, followed by C_3N_4-Au with a degradation rate of 81.1%, C_3N_4/10Pt with a degradation rate of 58.53% and C_3N_4 with a degradation rate of 53.50%. Au NPs as light absorber in C_3N_4-Au and C_3N_4-Au/10Pt can generate a large amount of high-energy hot e^- due to the plasma resonance effect and transfer them to the conduction band of C_3N_4 (Xixian et al., 2020, Dandan et al., 2021). The high electron affinity of Pt atoms as reductive cocatalysts in C_3N_4/10Pt and C_3N_4-Au/10Pt can promote electron transfer and inhibit e^--h^+ recombination. In this case, the electrons in the C_3N_4 conduction band are transferred to Pt through the Pt-N bond, which reduced the transfer distance and improved the charge separation (Yidong et al., 2021). In purpose to explore the effect of Pt amounts on photocatalyst degradation rate, 5, 10, 15 cycles of Pt precisely controlled by ALD were deposited on C_3N_4-Au surface, respectively. As illustrated in Fig.6b C_3N_4-Au/10Pt (86.3%) has a faster degradation rate than C_3N_4-Au-5Pt (49.86%) and C_3N_4-Au/15Pt (34.04%). The Pt clusters have optimal particle size through the competing effects of the Schottky barrier and Coulomb barrier charging energy on the charge transfer efficiency at the C_3N_4-Pt interface. This is because the Schottky barrier increases with the Pt cluster size, while the Coulomb blocking charge energy is decreasing (Yifat et al., 2017). The experimental results showed that C_3N_4-Au/10Pt photocatalysts doped with 0.21% gold and loaded with 0.26% platinum on C_3N_4 by photodeposition and ALD, respectively, had the most excellent photocatalytic degradation ability for RhB (see Fig. 6a, b, c, d and Table 1).

In order to further study the properties of the synthesized photocatalysts and compare their photocatalytic activity differences, the kinetic curves of various photocatalysts for the photocatalytic degradation of RhB were fitted and the first-order reaction rate constants (k) were calculated (as shown in Fig. 6c and Fig. 6d). Fig. 6c shown the fitted kinetic curves of degradation of RhB by four different photocatalysts within 0–30 min under simulated sunlight irradiation. Among them, C_3N_4-Au/10Pt photocatalyst had the largest slope of all the fitted curves, indicating an excellent reaction kinetics of its photocatalytic activity. The k values of C_3N_4-Au/10Pt, C_3N_4-Au, g-C_3N_4/10Pt and C_3N_4 were 6.73×10^{-2}, 5.47×10^{-2}, 2.84×10^{-2} and 2.45×10^{-2} min^{-1}, respectively (Fig. 6c). The precisely controlled C_3N_4-Au/10Pt exhibited the highest kinetic constant k (6.73×10^{-2} min^{-1}), 2.75 times as high as that of C_3N_4 (2.45×10^{-2} min^{-1}). Fig. 6d indicated the k values of C_3N_4-Au/5Pt, C_3N_4-Au/10Pt, C_3N_4-Au/15Pt were 2.37×10^{-2}, 6.73×10^{-2} and 1.33×10^{-2} min^{-1}, respectively. With the Pt ALD cycle numbers increasing from 5 to 10, the

active sites and the catalytic activity of C_3N_4-Au/nPt increased. But the catalytic site reached saturation when Pt ALD cycle numbers were 10. So, the 10 cycle numbers of Pt ALD is dispersed on C_3N_4 well, the catalytic activity of C_3N_4-Au/10Pt reached the best. However, with the Pt ALD cycles number further increasing, Pt accumulates on the surface of C_3N_4-Au and its catalytic activity decreased (Chien-Te et al., 2013). C_3N_4-Au/10Pt synthesized by ALD technology had the homogeneity dispersion, which increased the adsorption capacity of RhB and maximized the active sites.

The results indicated that the precisely controlled sub-nanometric C_3N_4-Au/10Pt photocatalysts with high photocatalytic activity have been successfully prepared by ALD, which may be ascribed to the synergistic effect of C_3N_4, Pt and Au NPs (Jia et al., 2019, Wei et al., 2020, Dandan et al., 2021). By comparing with the reported photocatalytic activities of most C_3N_4-based photocatalysts for degradation of RhB under sunlight, the C_3N_4-Au/10Pt photocatalysts precisely tailored by ALD in this research showed quite more excellent photocatalytic activities. The specific characteristics of photocatalytic activity of C_3N_4-Au/10Pt are shown in Table S1. In order to investigate the stability of photocatalytic degradation of RhB by C_3N_4-Au/10Pt, four photocatalytic degradation cycles were repeated under the same conditions. The results showed the degradation rate of RhB by C_3N_4-Au/10Pt after four cycles was still comparable to that of after the first cycle, which proved that the C_3N_4-Au/10Pt photocatalysts had high photocatalytic stability (see Fig. 7a). To further investigate the reusability and stability of C_3N_4-Au/10Pt photocatalysts, the XRD patterns of them before and after the 4th recycling test were also studied. From Fig. 7b, we can see there were no difference between before and after the 4th recycling tests, indicating excellent recyclability and reusability of C_3N_4-Au/10Pt photocatalysts.

3.3. Mechanism of photocatalytic degradation

Under the sunlight irradiation, photogenerated electrons (e^-) and holes (h^+) on the surface of the photocatalysts participate in the degradation reaction which leading to different photocatalytic degradation paths of RhB. In order to study the photocatalytic mechanisms of C_3N_4-Au/10Pt photocatalysts for RhB under the sunlight irradiation, AA, EDTA-2Na and IPA were used as scavengers of superoxide radicals($\dot{s}O_2^-$), h^+ and hydroxyl radicals($\dot{s}OH$), respectively. As shown in Fig. 8a, after adding of AA, the photocatalytic degradation rate of RhB decreased significantly and the reactions were inhibited, indicating that $\dot{s}O_2^-$ was the main active species in the degradation process. Interestingly, when EDTA-2Na was added, the degradation efficiency of RhB was slightly improved. This may be because EDTA-2Na trapped the holes, which reduced the recombination of electrons and holes and allowed more electrons to react with oxygen to produce $\dot{s}O_2^-$ active species (Xixian et al., 2020). In addition, the addition of IPA had little effect on the degradation of RhB. As a whole, $\dot{s}O_2^-$ is the main active species in the RhB degradation process by C_3N_4-Au/10Pt photocatalysts under the sunlight irradiation.

The degradation effect of C_3N_4-Au/10Pt under different conditions was studied in Fig. 8b. When N_2 was introduced in the reaction system, the degradation rate of RhB was only 19.62% after 30 min, indicating that the degradation of RhB
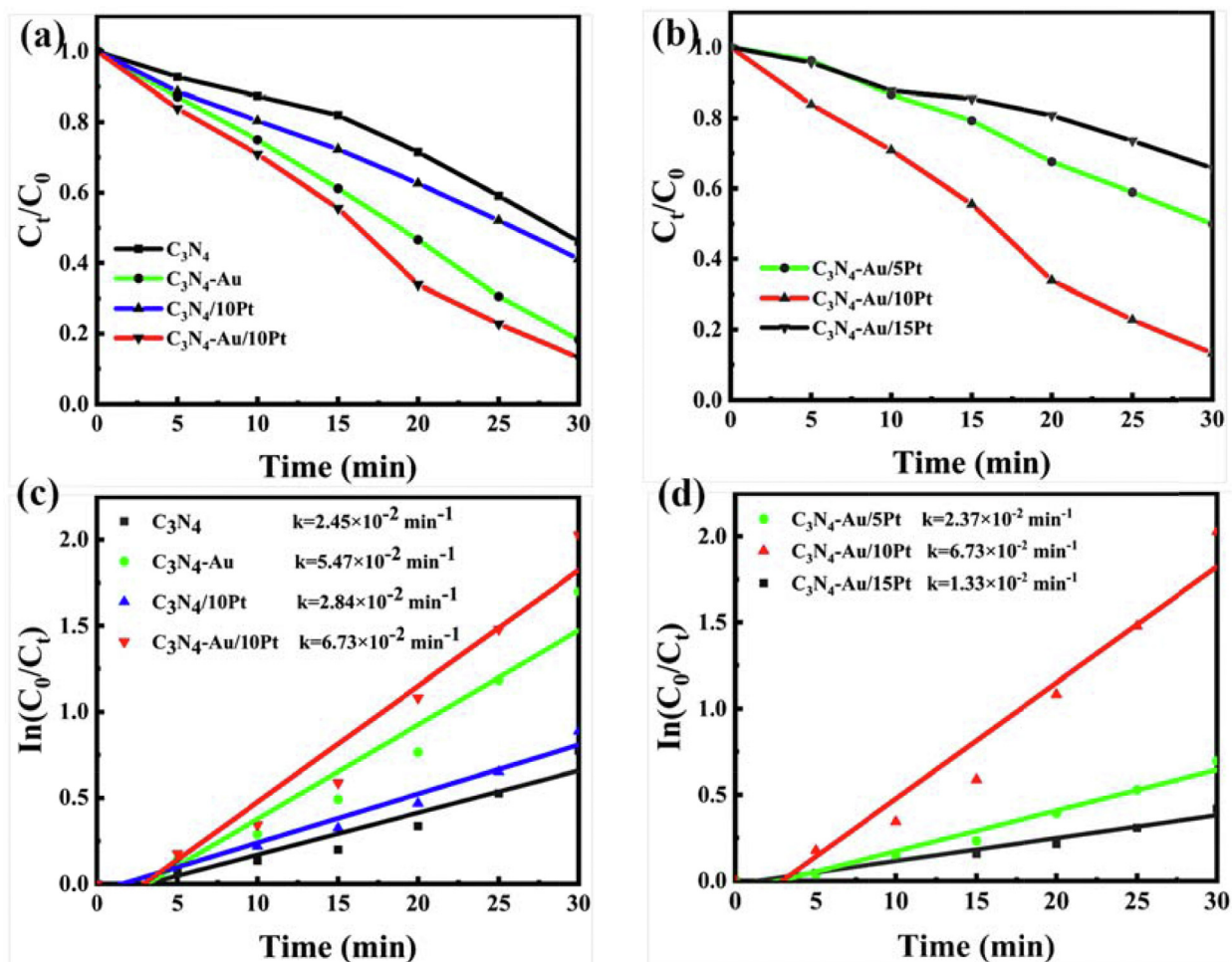
Fig. 6 RhB degradation curves (a, b) and ratios (c, d) by as-prepared different photocatalysts under visible light irradiation.
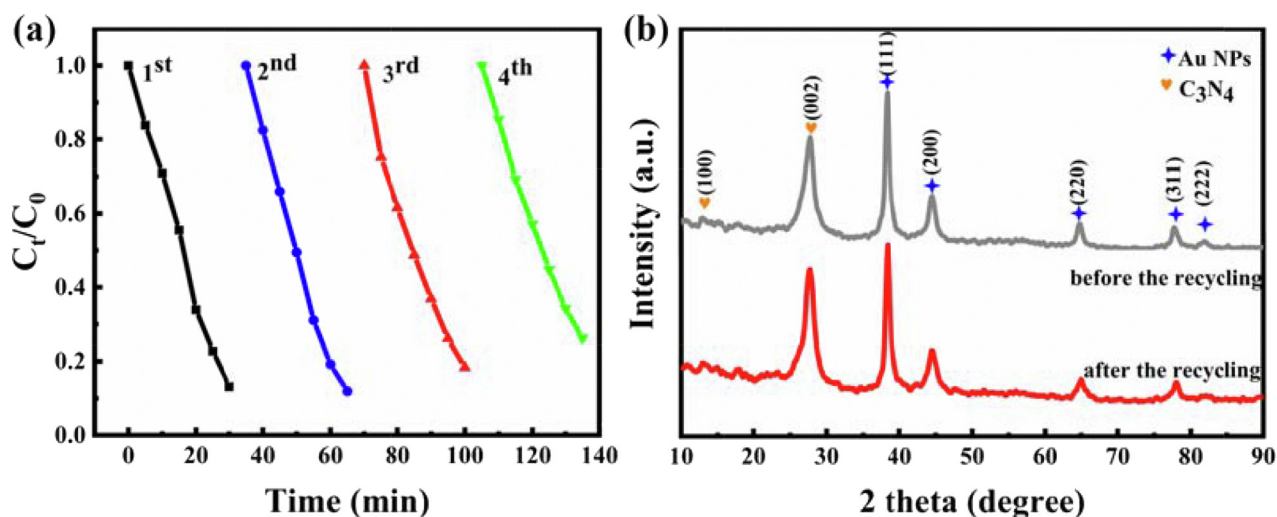

Fig. 7 Degradation stability of RhB by photocatalysts (a) and XRD patterns of C_3N_4-Au/10Pt before and after the 4th recycling (b).

was inhibited under N_2 condition. When O_2 was passed into RhB solution, the degradation rate of RhB was 87.2%, which is similar to the degradation rate in air. It is further proved that

$\dot{s}O_2^-$ is the main active species in the C_3N_4-Au/10Pt catalytic system under the sunlight irradiation and the oxygen content in the system (air) is enough for RhB degradation.
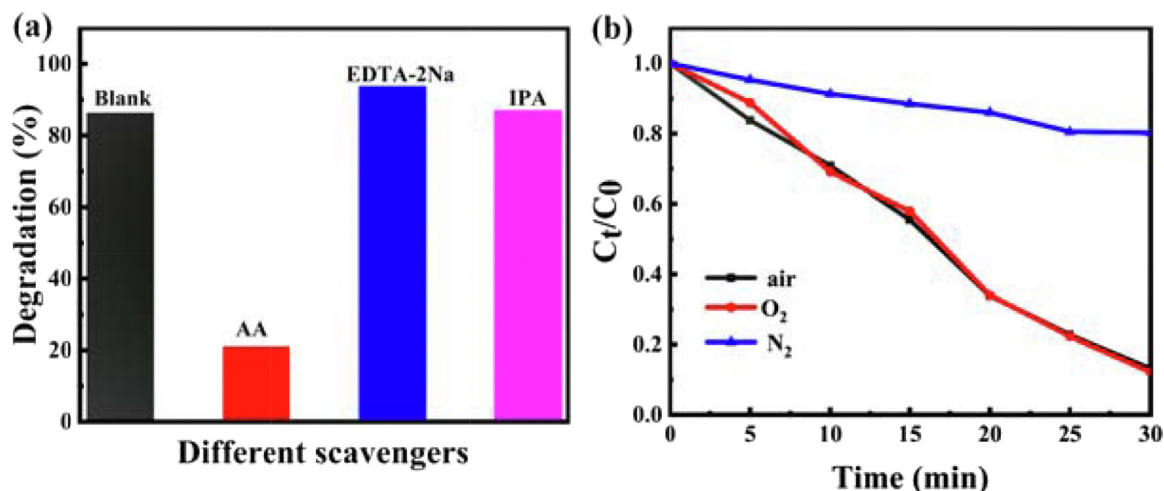
Fig. 8 Radicals trapping experiments (a) and degradation experiments of different gases (b) in C_3N_4-Au/10Pt/sunlight system.

By studying the electronic band structure of C_3N_4 and C_3N_4-Au/10Pt, the catalytic degradation mechanism of C_3N_4-Au/10Pt photocatalysts can be further explained. The following empirical formulas are used to estimate the E_{VB} and E_{CB} of photocatalytic materials (Zhixiao et al., 2017, Taiping et al., 2018):

$$E_{VB} = \chi - E_c + 0.5E_g \qquad (4)$$

$$E_{CB} = E_{VB} - E_g \qquad (5)$$

where E_{VB} and E_{CB} represent the valence band and conduction band of the photocatalysts, respectively. χ is the Mulliken electronegativity (the value of C_3N_4 and C_3N_4-Au/10Pt are about 4.72 eV and 5.26 eV vs. NHE, separately, the following band gap energy all vs. NHE) (Hao et al., 2021). E_c is the energy of a free electron on the hydrogen scale estimated to be 4.5 eV (Xixian et al., 2020, Hao et al., 2021). E_g is band gap energy of a semiconductor (E_g of C_3N_4 and C_3N_4-Au/10Pt are 2.87 eV and 2.94 eV, respectively). According to the above formulas, the E_{VB} and E_{CB} values of C_3N_4 are calculated to be + 1.66 eV and −1.21 eV, respectively, while the values of C_3N_4-Au/10Pt are + 2.23 eV and −0.71 eV, respectively.

Based on the conclusions above mentioned, the photocatalytic mechanism of C_3N_4-Au/10Pt photocatalysts for efficient degradation of RhB under sunlight is shown in Fig. 9. When C_3N_4-Au/10Pt under the irradiation of sunlight, the electrons in the E_{VB} of C_3N_4 are excited and jump to the E_{CB}, leaving h^+ in the E_{VB}. At the same time, Au NPs in C_3N_4-Au/10Pt can generate a large amount of high-energy hot e^- due to the plasma resonance effect and transfer them to the conduction band of C_3N_4 (Xixian et al., 2020, Dandan et al., 2021). The high electron affinity of Pt atoms in C_3N_4-Au/10Pt can promote electron transfer and inhibit e^--h^+ recombination. In this case, the electrons in the C_3N_4 conduction band are transferred
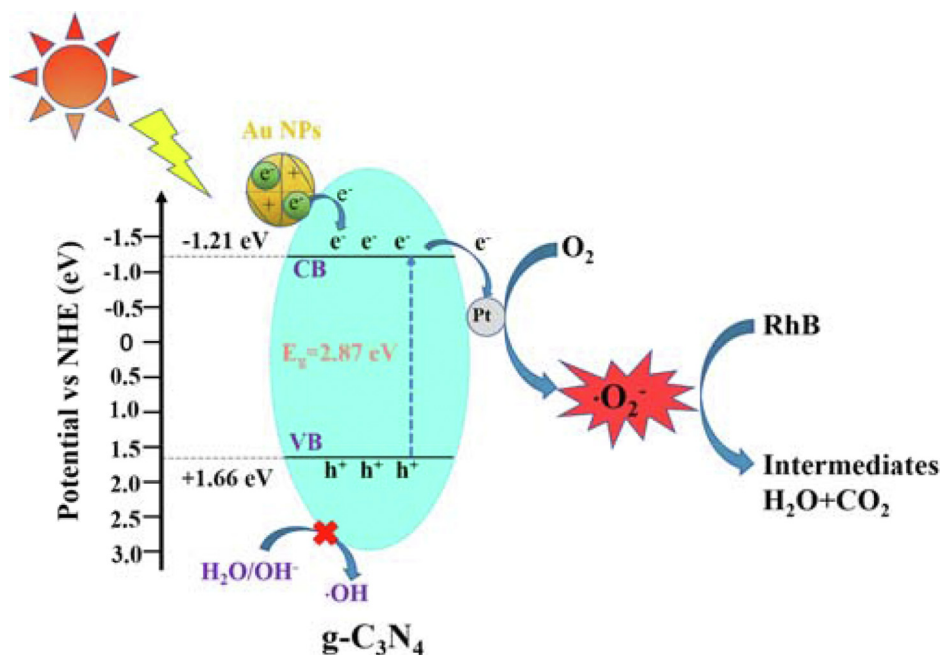

Fig. 9 The mechanism of photocatalytic degradation of RhB by C_3N_4-Au/10Pt photocatalysts under sunlight.

to Pt through the Pt-N bond, which reduced the transfer distance and improved the charge separation (Yidong et al., 2021). Furthermore, the carrier separation efficiency is improved by forming Schottky Barrier in the contact between Pt and g-C_3N_4. Because the C_3N_4-Au/10Pt conduction potential (-0.71 eV) is more negative than that of O_2/O_2^- (-0.33 eV) reduction potential, a large number of photogenerated electrons react with O_2 absorbed on the C_3N_4-Au/10Pt surface to generate the active radical $\dot{s}O_2^-$, which leads to the efficient degradation of RhB (Mingjuan et al., 2019). Since the value of E_{VB} in C_3N_4 (+1.17 eV) is more negative than the potentials of $OH^-/\dot{s}OH$ (+1.99 eV) and $H_2O/\dot{s}OH$ (+2.27 eV) (Chao et al., 2020, Bo et al., 2021), the h^+ generated by C_3N_4-Au/10Pt cannot react with H_2O to form $\dot{s}OH$. So, the degradation mechanism of RhB by C_3N_4-Au/10Pt photocatalysts are shown as follows:

$$C_3N_4 - Au/10Pt + h\nu \rightarrow e^- + h^+$$

$$e^- + O_2 \rightarrow .O_2^-$$

$$.O_2^- + RhB \rightarrow CO_2 + H_2O$$
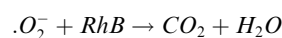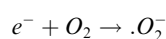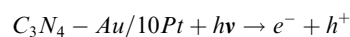
4. Conclusion

In summary, the new precisely regulated C_3N_4-Au/nPt photocatalysts were successfully synthesized by ALD. Under simulated sunlight irradiation, the degradation rate of 10 mg/L RhB (100 mL) by 1.5 mg C_3N_4-Au/10Pt catalysts was 100% within 65 min, which is much better than other photocatalysts for the degradation of RhB. Pt clusters and Au NPs synergistically promoted the photocatalytic degradation of C_3N_4 by Schottky barrier and LSPR, respectively. The degradation mechanism of RhB by C_3N_4-Au/10Pt was demonstrated that $\cdot O_2^-$ was the main active species in the photocatalytic process. This work highlights that an easy and controllable method can be used to prepare a "two in one" high-efficiency photocatalysts by ALD, which open up a new method to tailor and fabricate highly active photocatalysts in solving the energy crisis and environmental pollution.

Acknowledgments

Appendix A. Supplementary material

Supplementary data to this article can be found online at https://doi.org/10.1016/j.arabjc.2022.103951.

References

Amene, N., Morasae, S., Ali, P., et al, 2017. Graphitic carbon nitride (g-C_3N_4)-based photocatalysts for solar hydrogen generation: recent advances and future development directions. J. Mater. Chem. A 5, 23406–23433.

Bo, L., Mengying, L., Wei, J., et al, 2021. Self-photoreduced Ag0-doped Ag(I)–organic frameworks with efficient visible-light-driven photocatalytic performance. CrystEngComm 23, 7496–7501.

Chao, L., Zitong, H., Yue, F., et al, 2020. Ultrathin Z-scheme 2D/2D N-doped HTiNbO$_5$ nanosheets/g-C_3N_4 porous composites for efficient photocatalytic degradation and H_2 generation under visible light. J. Colloid Interface Sci., 58358–58370

Chien-Te, H., Yung-Ying, L., Dong-Ying, T., et al, 2013. Platinum electrocatalysts attached to carbon nanotubes by atomic layer deposition with different cycle numbers. J. Taiwan Inst. Chem. Eng. 45, 186–191.

Chuang, H., Quan, Q., Hao Ming, C., et al, 2017. Progressive Design of Plasmonic Metal-Semiconductor Ensemble toward Regulated Charge Flow and Improved Vis–NIR-Driven Solar-to-Chemical Conversion. Small. 13, 1602947.

Dandan, W., Yuhan, L., Bo, Y., et al, 2021. Improved visible-light driven photocatalysis by loading Au onto C_3N_4 nanorods for degradation of RhB and reduction of CO_2. Adv. Powder Technol. 32, 1653–1662.

Dilshad, M., M. Yuanyu and R. Sohrab, 2017. Graphitic C_3N_4 based noble-metal-free photocatalyst systems: A review. Appl. Catal. B Environm. 206556–206588.

Eshwar, R., Ronald, E.B., Carole, S., et al, 2020. Achieving Net Zero Energy Greenhouses by Integrating Semitransparent Organic Solar Cells. Joule. 4, 490–506.

Fan, D., Zaiwang, Z., Ting, X., et al, 2013. In Situ Construction of g-C_3N_4/g-C_3N_4 Metal-Free Heterojunction for Enhanced Visible-Light Photocatalysis. ACS Appl. Mater. Interfaces 5, 11392–11401.

Guohui, D., L. J. Daniel, Z. Ling, et al., 2017. Carbon vacancy regulated photoreduction of NO to N_2 over ultrathin g-C_3N_4 nanosheets. Appl. Catal. B Environm. 218515–218524.

Hao, H., Yu-Xuan, L., Hui-Long, W., et al, 2021. In situ fabrication of ultrathin-g-C_3N_4/AgI heterojunctions with improved catalytic performance for photodegrading rhodamine B solution. Appl. Surf. Sci. 538, 148132.

Ji-Xiao, Z., Chao-Qiu, C., Cai-Hong, X., et al, 2020. Selectivity Regulation in Au-Catalyzed Nitroaromatic Hydrogenation by Anchoring Single-Site Metal Oxide Promoters. ACS Catal. 10, 2837–2844.

Jia, Z., Lyu, F., Zhang, L.C., et al, 2019. Pt nanoparticles decorated heterostructured g-C_3N_4/Bi$_2$MoO$_6$ microplates with highly enhanced photocatalytic activities under visible light. Sci. Rep. 9, 7636.

Jiankang, Z., Zhe, G., Sen, W., et al, 2019. Origin of synergistic effects in bicomponent cobalt oxide-platinum catalysts for selective hydrogenation reaction. Nat. Commun. 10, 4166.

Jie, Y., Wenzhao, F., Chaoqiu, C., et al, 2021. Atomic Design and Fine-Tuning of Subnanometric Pt Catalysts to Tame Hydrogen Generation. ACS Catal. 11, 4146–4156.

Jingqi, T., Qian, L., Abdullah, M.A., et al, 2013. Ultrathin graphitic carbon nitride nanosheets: a novel peroxidase mimetic, Fe doping-mediated catalytic performance enhancement and application to rapid, highly sensitive optical detection of glucose†. Nanoscale. 5, 11604–11609.

Jingrun, R., Weiwei, G., Hailong, W., et al, 2018. Metal-Free 2D/2D Phosphorene/g-C_3N_4 Van der Waals Heterojunction for Highly Enhanced Visible-Light Photocatalytic H_2 Production. Adv. Mater. 30, e1800128.

Jinjuan, X., Shuaishuai, M., Yuming, Z., et al, 2015. Facile Photochemical Synthesis of Au/Pt/g-C_3N_4 with Plasmon-Enhanced Photocatalytic Activity for Antibiotic Degradation. ACS Appl. Mater. Interfaces 7, 9630–9637.

Jinlong, G., Can, L., Michael, R.W., 2019. Advances in solar energy conversion. Chem. Soc. Rev. 48, 1862–1864.

Juan, L., Yang, L., Naiyun, L., et al, 2015. Metal-free efficient photocatalyst for stable visible water splitting via a two-electron pathway. Science 46, 970–974.

Kwun-Han, W., Yu-Jie, H., Hsisheng, T., 2017. Oligomer-Incorporated Polymeric Layer Framework of Graphitic Carbon Nitride for Effective Photocatalytic Hydrogen Evolution. Part. Part. Syst. Char. 35, 1700221.

Li, Y., Jingyang, H., Tiantian, L., et al, 2021. Tremella-like integrated carbon nitride with polyvinylimine-doped for enhancing photocatalytic degradation and hydrogen evolution performances. Sep. Purif. Technol. 279, 119766.

Liu, J., Zhang, T., Wang, Z., 2011. Simple pyrolysis of urea into graphitic carbon nitride with recyclable adsorption and photocatalytic activity. J. Mater. Chem. A 21, 14398–14401.

Mamba, G., Mishra, A.K., 2016. Graphitic carbon nitride (g-C$_3$N$_4$) nanocomposites: A new and exciting generation of visible light driven photocatalysts for environmental pollution remediation. Environmental, Applied Catalysis B, pp. 198347–198377.

Meng, X., L. Liu, S. Ouyang, et al., 2016. Nanometals for Solar-to-Chemical Energy Conversion: From Semiconductor-Based Photocatalysis to Plasmon-Mediated Photocatalysis and Photo-Thermocatalysis Advanced Materials. 28, 6781–6803.

Min-Ying, T., Natalie, E.P., Lisa, J.G., et al, 2012. Enhanced Photocatalytic Hydrogen Generation Using Polymorphic Macroporous TaON. Adv. Mater. 24, 3406–3409.

Mingjuan, Z., Yi, Z., Lin, T., et al, 2019. Ultrathin Bi$_2$WO$_6$ nanosheets loaded g-C$_3$N$_4$ quantum dots: A direct Z-scheme photocatalyst with enhanced photocatalytic activity towards degradation of organic pollutants under wide spectrum light irradiation. J. Colloid Interface Sci., 539654–539664

Mohammed, M., Zakaria, A., Abdallah, A., 2020. Emerging Chemical Functionalization of g-C$_3$N$_4$: Covalent/Noncovalent Modifications and Applications. ACS Nano 14, 12390–12469.

Ning, D., Longshuai, Z., Muneaki, H., et al, 2017. Enhanced photocatalytic activity of mesoporous carbon/C$_3$N$_4$ composite photocatalysts. J. Colloid Interface Sci. 512, 474–479.

Ningyan, C., Jingqi, T., Qian, L., et al, 2013. Au-Nanoparticle-Loaded Graphitic Carbon Nitride Nanosheets: Green Photocatalytic Synthesis and Application toward the Degradation of Organic Pollutants. ACS Appl. Mater. Interfaces 5, 6815–6819.

Noor Izzati Md, R., L. Sze-Mun, S. Jin-Chung, et al., 2021. Fabrication of Z-scheme rod-like Ag$_2$Mo$_2$O$_7$/g-C$_3$N$_4$ for phenol degradation under IO^{4}/visible light system. Mater. Lett. 294, 129791.

Noor Izzati Md, R., L. Sze-Mun, S. Jin-Chung, et al., 2022. Comparative study of g-C$_3$N$_4$/Ag-based metals (V, Mo, and Fe) composites for degradation of Reactive Black 5 (RB5) under simulated solar light irradiation. J. Environ. Chem. Eng. 10, 107308.

Po, W., Jiarui, W., Jing, Z., et al, 2014. Structure defects in g-C$_3$N$_4$ limit visible light driven hydrogen evolution and photovoltage†. J. Mater. Chem. A 2, 20338–20344.

Seung Jun, L., Talshyn, B., Hyeon Jin, J., et al, 2020. Plasmonic ZnO/Au/g-C$_3$N$_4$ nanocomposites as solar light active photocatalysts for degradation of organic contaminants in wastewater. Chemosphere 263, 128262.

Shaowen, C., Jing, J., Bicheng, Z., et al, 2016. Shape-dependent photocatalytic hydrogen evolution activity over a Pt nanoparticle coupled g-C$_3$N$_4$ photocatalyst†. PCCP 19457.

Sibo, C., Y. Siyuan, S. Xiaolin, et al., 2019. Carbon-Coated Cu nanoparticles as a Cocatalyst of g-C$_3$N$_4$ for Enhanced Photocatalytic H$_2$ Evolution Activity under Visible-Light Irradiation. Energy Technol. 7, 1800846–1800846.

Surendar, T., Santosh, K., Syam, K., et al, 2014. Fe-doped and -mediated graphitic carbon nitride nanosheets for enhanced photocatalytic performance under natural sunlight†. J. Mater. Chem. A 2, 6772–6780.

Taehwan, J., Huiyan, P., Sangwoo, P., et al, 2019. Atomic and electronic structures of graphene-decorated graphitic carbon nitride (g-C$_3$N$_4$) as a metal-free photocatalyst under visible-light. Appl. Catal. B 256, 117850.

Taiping, H., Pengfei, L., Jinfeng, Z., et al, 2018. Highly efficient direct Z-scheme WO$_3$ /CdS-diethylenetriamine photocatalyst and its enhanced photocatalytic H$_2$ evolution under visible light irradiation. Appl. Surf. Sci. 442, 20–29.

Trishamoni, K., Sritam, B., Shahnaz, A., et al, 2021. Plasmon Activation versus Plasmon Quenching on the Overall Photocatalytic Performance of Ag/Au Bimetal Decorated g-C$_3$N$_4$ Nanosheets Under Selective Photoexcitation: A Mechanistic Understanding with Experiment and Theory. Appl. Catal. B 298, 120614.

Wee-Jun, O., Lling-Lling, T., Siang-Piao, C., et al, 2015. Surface charge modification via protonation of graphitic carbon nitride (g-C$_3$N$_4$) for electrostatic self-assembly construction of 2D/2D reduced graphene oxide (rGO)/g-C$_3$N$_4$ nanostructures toward enhanced photocatalytic reduction of carbon dioxide to methane. Nano Energy 13, 757–770.

Wee-Jun, O., Lling-Lling, T., Yun Hau, N., et al, 2016. Graphitic Carbon Nitride (g-C$_3$N$_4$)-Based Photocatalysts for Artificial Photosynthesis and Environmental Remediation: Are We a Step Closer To Achieving Sustainability? Chem. Rev. 116, 7159–7329.

Wei, Z., Sisi, M., Gang, Y., et al, 2020. Z-scheme Au decorated carbon nitride/cobalt tetroxide plasmonic heterojunction photocatalyst for catalytic reduction of hexavalent chromium and oxidation of Bisphenol A. J. Hazard. Mater. 124539.

Wenjun, Z., Datong, X., Fengjue, W., et al, 2021. AgCl/Au/g-C$_3$N$_4$ ternary composites: Efficient photocatalysts for degradation of anionic dyes. J. Alloy. Compd. 868, 159266.

Xiaogang, L., Wentuan, B., Lei, Z., et al, 2016. Single-Atom Pt as Co-Catalyst for Enhanced Photocatalytic H$_2$ Evolution. Adv. Mater. 28, 2427–2431.

Xin, L., Chongyang, L., Dongyao, W., et al, 2019. Improved charge transfer by size-dependent plasmonic Au on C$_3$N$_4$ for efficient photocatalytic oxidation of RhB and CO$_2$ reduction. Chin. J. Catal. 40, 928–939.

Xinchen, W., Xiufang, C., Arne, T., et al, 2009. Metal-Containing Carbon Nitride Compounds: A New Functional Organic-Metal Hybrid Material. Adv. Mater. 21, 1609–1612.

Xixian, H., Nengwu, Z., Fulin, M., et al, 2020. Novel Au@C modified g-C$_3$N$_4$ (Au@C/g-C$_3$N$_4$) as efficient visible-light photocatalyst for toxic organic pollutant degradation: Synthesis, performance and mechanism insight. Sep. Purif. Technol. 252, 117485.

Xu, D., Dandan, W., Hongji, L., et al, 2021. Boosting interfacial charge separation and photocatalytic activity of 2D/2D g-C$_3$N$_4$/ZnIn$_2$S$_4$ S-scheme heterojunction under visible light irradiation. J. Alloy. Compd. 162209.

Ya-Nan, L., Cong-Cong, S., Nan, J., et al, 2017. g-C$_3$N$_4$ Hydrogen-Bonding Viologen for Significantly Enhanced Visible-Light Photocatalytic H$_2$ Evolution. ACS Catal. 7, 8228–8234.

Yan, W., Dandan, W., Hongji, L., et al, 2021. Enhanced photocatalytic hydrogen evolution of 2D/2D N-Sn$_3$O$_4$/g-C$_3$N$_4$ S-scheme heterojunction under visible light irradiation. Appl. Surf. Sci. 567, 150903.

Yanchun, D., Jun, L., Yanbin, H., et al, 2020. Engineering the Photocatalytic Behaviors of g/C$_3$N$_4$-Based Metal-Free Materials for Degradation of a Representative Antibiotic. Adv. Funct. Mater. 30, 2002353.

Yidong, H., Yunteng, Q., Yansong, Z., et al, 2021. Single Pt atom-anchored C$_3$N$_4$: A bridging Pt−N bond boosted electron transfer for highly efficient photocatalytic H$_2$ generation. Chem. Eng. J. 412, 128749.

Yifat, N., Yair, M., Yonatan, D., et al, 2017. Size Matters: Cocatalyst Size Effect on Charge Transfer and Photocatalytic Activity. Nano Lett. 18, 357–364.

Yiping, F., Mengyao, S., Zhijie, X., et al, 2020. Photochemical transformation of C$_3$N$_4$ under UV irradiation: Implications for environmental fate and photocatalytic activity. J. Hazard. Mater. 394, 122557.

Yong, X., Yong, C., Wen-Fu, F., 2018. Visible-light driven oxidative coupling of amines to imines with high selectivity in air over core-shell structured CdS@C_3N_4. Appl. Catal. B 236, 176–183.

Yuan, T., Xiaohong, Y., Manman, M., et al, 2020. Anatase TiO_2@-MIL-101(Cr) nanocomposite for photocatalytic degradation of bisphenol A. Colloids Surf., A 596, 124745.

Yuyang, K., Yongqiang, Y., Li-Chang, Y., et al, 2015. An Amorphous Carbon Nitride Photocatalyst with Greatly Extended Visible-Light-Responsive Range for Photocatalytic Hydrogen Generation. Adv. Mater. 27, 4572–4577.

Zhe, G., Yong, Q., 2017. Design and Properties of Confined Nanocatalysts by Atomic Layer Deposition. Acc. Chem. Res. 50, 2309–2316.

Zhengxin, D., Xiufang, C., Markus, A., et al, 2010. Synthesis of Transition Metal-Modified Carbon Nitride Polymers for Selective Hydrocarbon Oxidation. ChemSusChem 4, 274–281.

Zhi Wei, S., Shuhua, L., Michelle, L., et al, 2012. Janus Au-TiO_2 Photocatalysts with Strong Localization of Plasmonic Near-Fields for Efficient Visible-Light Hydrogen Generation. Adv. Mater. 24, 2310–2314.

Zhixiao, Q., Yubin, C., Zhenxiong, H., et al, 2017. A bifunctional NiCoP-based core/shell cocatalyst to promote separate photocatalytic hydrogen and oxygen generation over graphitic carbon nitride. J. Mater. Chem. A 5, 19025–19035.